Journal of Materials Chemistry A

Accepted Manuscript

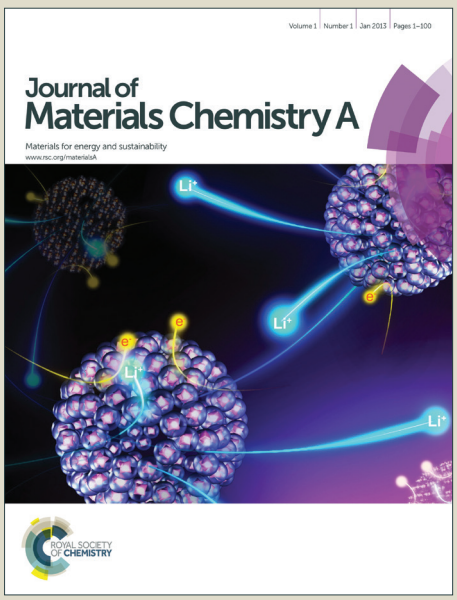

ROYAL SOCIETY OF CHEMISTRY

www.rsc.org/materialsA

Hierarchical $NiCo_2O_4$ Nanosheets@Hollow Microrod Arrays for High-Performance Asymmetric Supercapacitors

Xue-Feng Lu, Dong-Jun Wu, Run-Zhi Li, Qi Li, Sheng-Hua Ye, Ye-Xiang Tong and Gao-Ren Li*

MOE Laboratory of Bioinorganic and Synthetic Chemistry, KLGHEI of Environment and Energy Chemistry, School of Chemistry and Chemical Engineering, Sun Yat-sen University, Guangzhou 510275, China

*E-mail: ligaoren@mail.sysu.edu.cn

ABSTRACT

Novel hierarchical $NiCo_2O_4$ nanosheets@hollow microrod arrays (NSs@HMRAs) are fabricated by a sim-ple and environmental friendly template-assised electrodeposition followed by thermal annealing. Due to their unique nanostructures, the $NiCo_2O_4$ NSs@HMRAs as electrodes exhibited high specific capacitance (C_{sp}) (678 F/g at 6 A/g) and outstanding cycle stability (C_{sp} retention of 96.06% after 1500 cycles). The desirable superior capacitive performance of the $NiCo_2O_4$ NSs@HMRAs can be attributed to the large specific surface area, fast ion diffusion, and perfect charge transmission in the hierarchical NSs@HMRAs. The asymmetric supercapacitor (ASC) based on the $NiCo_2O_4$ NSs@HMRAs as positive electrode and active carbon (AC) as negative electrode was assembled and it exhibited a C_{sp} of 70.04 F/g at 5 mV/s and a high energy density of 15.42 Wh/kg. Moreover, the $NiCo_2O_4$ NSs@HMRAs//AC ASC has an outstand-ing cycle stability (almost no C_{sp} loss after 2500 cycles), making it promising as one of the most attractive candidates for electrochemical energy storage.

Keywords: Electrodeposition; $NiCo_2O_4$; Nanosheet; Hollow microrod; Asymmetric supercapacitor

Introduction

The growing concerns about air pollution and global warming and the decreasing availability of fossil fuels call for not only urgent development of clean alternative energies but also more advanced energy storage devices. Recently, supercapacitors (SCs) with desirable properties of fast charging (with seconds), high power density (10 times more power than batteries) and excellent cycling stability (more than 1000 cycles) have become some of the most promising candidates for next-generation energy storage devices.[1-5] Based on the charge storage mechanism, SCs are classified into electrical double layer capacitors (EDLCs) and pseudocapacitors, where the charge is stored using the redox-based Faradaic reactions.[6-11] As to the pseudocapacitors, the electrode materials possessing multiple oxidation states/structures that enable rich redox reactions for pseudocapacitance generation are desirable for performance enhancement.[12] Recently, a low-cost binary metal oxide, spinel $NiCo_2O_4$, has sparked worldwide concern as appealing pseudocapa-citive electrodes for advanced SCs because of the presence of Ni^{2+}/Ni^{3+} and Co^{2+}/ Co^{3+} redox couples in such spinel cobaltite.[13-22]

Nanomaterials, particularly hollow nanostructures, could play critical roles to improve the performances of energy storage devices.[23-25] With large surface area and short diffusion path for electrons and ions, hollow nanostructures are well suited architectures for high-performance SC electrodes.[26-30] Hollow nano-structures with higher complexity are expected to offer exciting opportunities for both fundamental studies and practical applications. For example, hierarchically structured TiO_2 nanotube arrays composed of anatase and rutile nanocrystals exhibited a markedly enhanced power conversion efficiency compared to simple nanotube arrays.[31] With this interest, researchers worldwide have recently devoted rapidly increasing attention to the rational design and fabrication of complex hollow nanostructures.[32-33] Hierarchically hollow nanorod arrays can be considered as the special hollow nanostructures that might own the benefits from both hollow and 1D nanostructures. However, there has been less development in the fabrication of complex 1D hollow nanorod arrays although great advances in complex hollow structures with isotropic architectures. Therefore, it is highly desirable to develop a simple strategy to effectively fabricate novel and highly complex 1D hollow nanorod arrays for SC application.

In light of the above ideas, the novel $NiCo_2O_4$ nanosheets@hollow microrod arrays (NSs@HMRAs) are directly fabricated on the conductive substrate for SC application via a facile electrodeposition using ZnO microrods arrays (MRAs) as template, followed by calcination in air. The prepared $NiCo_2O_4$ NSs@HMRAs simultaneously possess binary redox couples of Ni^{2+}/Ni^{3+} and Co^{2+}/Co^{3+}, large specific surface area, nanosheet networks, porous nanostructures, hollow microrod arrays and excellent electrical contact with current collector. The electrochemical measurements demonstrated novel $NiCo_2O_4$ NSs@HMRAs exhibited high supercapacitive performances and long-term cycle stability, indicating potential applications as high-performance SC electrodes. Furthermore, the asymmetric supercapacitor (ASC) based on the $NiCo_2O_4$ NSs@HMRAs as positive electrode and active carbon (AC) as negative electrode exhibits a high C_{sp} of 70.04 F/g at 5 mV/s and high energy density of 15.42 Wh/kg. Moreover, it shows an outstanding cycling stability (almost no C_{sp} loss after 2500 cycles), making it promising as one of the most attractive candi-dates for energy storage.

Experimental section

Synthesis of $NiCo_2O_4$ NSs@HMRAs: All chemical reagents used in this study were analytical (AR) grade. Electrodeposition was carried out in a simple two-electrode cell via galvanostatic electrolysis and the graphite electrode was used as a counter electrode (spectral grade, 1.8 cm^2). Ti thin plates (99.99%, 2.5 cm^2) were used as the conductive substrates for electrodeposition and they were prepared complying the following steps before each experiment: firstly polished by SiC abrasive paper from 300 to 800 grits, then dipped in HCl solution (5%) for 10 min and rinsed with acetone in ultrasonic bath for 5 min, and finally washed by distilled water. ZnO microrod arrays (MRAs) as template was firstly electrodeposited on Ti substrate in solution of 0.01 M $Zn(NO_3)_2$+0.05 M NH_4NO_3 with current density of 0.5 $mA \cdot cm^{-2}$ at 70 °C for 90 min. ZnO@$Ni(OH)_2$/$Co(OH)_2$ MRAs was then fabricated by the electrodeposition of $Ni(OH)_2$/$Co(OH)_2$ composites on the surfaces of ZnO MRAs in solution of 1.5 mM $Ni(NO_3)_2$+3 mM $Co(NO_3)_2$+4.5 mM NH_4NO_3 +10%(percent by volume) dimethyl sulfoxide (DMSO) with current density of 0.05 $mA \cdot cm^{-2}$ at 30 °C for 90 min. Finally, the $NiCo_2O_4$ NSs@HMRAs were fabricated after

dissolving ZnO MRAs template in sodium hydroxide solution (3.0 M) and annealing in air at 300 °C for 2 h with a heating rate of 5 °C/min. During the calcination, the $NiCo_2O_4$ was formed via the following reaction:

$$2Ni(OH)_2 + 4Co(OH)_2 + O_2 \rightarrow 2NiCo_2O_4 + 6H_2O \quad (1)$$

Material characterization: The morphologies, microstructures, and compositions of the products were characterized by field-emission scanning electron microscopy(FE-SEM, JSM-6330F), X-ray diffractometry (XRD, D8ADVANCE), transmission electron microscopy (TEM, Tecnai™ G2 F30), and photoelectron Spectroscopy (XPS, ESCALab250). The inductively coupled plasma atomic emission spectroscopy (ICP, SPECTRO) was used to analyze the loading of $NiCo_2O_4$ NSs@HMRAs.

Electrochemical characterization: Electrochemical measurements of the $NiCo_2O_4$ NSs@HMRAs were carried out in a standard three-electrode electrolytic cell in 1.0 M KOH aqueous solution. A graphite electrode was used as a counter electrode. A saturated calomel electrode (SCE) was used as the reference electrode. The working electrode was impregnated with the electrolyte for 30 min to ensure the nanocomposite electrode was thoroughly wet and then actived in small current with chronopotentiometric.

Cyclic voltammometry and chronopotentiometric measurements were performed on a CHI 760 D electrochemical workstation (CH instruments, Inc.) to determine the electrochemical properties. The average specific capacitance (C_{sp}) determined from the cyclic voltammograms (CVs) were calculated according to Eq. (2):

$$C_{sp} = \frac{1}{w\Delta V}\int_y^x i\,dt \quad (2)$$

Where i, ΔV and w were the current (mA), the voltage range of one scanning segment (V), and weight of electrode material (mg), respectively. The C_{sp} was also calculated from the chronopotentiometric curves according to Eq. (3):

$$C_{sp} = \frac{I\Delta t}{w\Delta V} \quad (3)$$

$$d_e = \frac{1}{2}C_{sp}(\Delta V)^2 \quad (4)$$

$$d_p = \frac{d_e}{\Delta t} \quad (5)$$

Where I was the charge/discharge current, Δt was the time for a full charge or discharge, w was the mass of the active electrode material, and ΔV was the voltage change after a full charge/discharge.

Asymmetric supercapacitors (ACSs): ASCs were assembled based on the $NiCo_2O_4$ NSs@HMRAs (0.17 mg) as positive electrodes, the active carbon (AC) (0.55 mg) as negative electrodes, and the TF45 (NKK) membrane as separators. The negative electrode was prepared as follows: firstly, the AC, acetylene black and polyte-trafluoroethylene (PTFE) powers with mass proportions (%) of 80:10:10 were dispersed in 1-Methyl-2-pyrrolidinone (NMP) to produce a homogeneous paste by magnetic stirring. Then the resulting mixture was coated onto nickel foam substrate (1.0 cm × 3.0 cm) by a spatula. Finally, the fabricated elec-trode was pressed and then dried at 120 ^{0}C for 24 h. The mass ratio of negative electrode (AC) to positive electrode was decided according to the well-known charge balance theory (q^+=q^-).[15] The ASC was meas-ured with a two-electrode system in 1.0 M KOH aqueous solution. In the relationship, the charge stored by each electrode usually depends on the specific capacitance (C_{sp}), the potential window (ΔV) and the mass of active material (m), as is shown in the equation (4):[34]

$$q = C_{sp} \times \Delta V \times m \quad (6)$$

In order to obtain q^+=q^-, the mass balancing will be expressed as the equation (5):[34]

$$\frac{m^+}{m^-} = \frac{C_{sp}^- \times \Delta V_-}{C_{sp}^+ \times \Delta V_+} \quad (7)$$

C_{sp}^+ and C_{sp}^- is the C_{sp} of $NiCo_2O_4$ NSs@HMRAs and AC electrodes, respectively. ΔV_+ and ΔV_- is the voltage range of one scanning segment (V) of $NiCo_2O_4$ NSs@HMRAs and AC electrodes, respectively. The optimal mass ratio between the $NiCo_2O_4$ NSs@HMRAs and AC electrodes is calculated to be about $m^+/m^- \approx 0.3$ in the ASC.

Results and discussion

SEM images of ZnO MRAs with different magnifications are shown in Figure 1a-b, which shows the hexagonal ZnO microrods are fabricated. The diameters of ZnO microrods are 250~300 nm, and the lengths are ~2.0 μm. SEM images of the ZnO@$Ni(OH)_2$/$Co(OH)_2$ MRAs with different magnifications are shown in Figure 1c-d, which shows ZnO microrods have uniform $Ni(OH)_2$/$Co(OH)_2$ composite wraps

and the array morphologies are kept very well. After dissolving ZnO MRAs and annealing in air at 300 °C for 2 h, the $NiCo_2O_4$ nanosheets@hollow microrod arrays (NSs@HMRAs) were fabricated and their SEM images with different magnifications are shown in Figure 1e-f. The average diameters of hierarchical $NiCo_2O_4$ microrods are in the range of 500~600 nm. To prove the NSs@HMRAs superstructures, TEM images were measured and they are shown in Figure 2a-c. The TEM image with low-magnification demonstrates the microrods are hollow and a large number of thin nanosheets grew on the surfaces of hollow microrods as shown in Figure 2a. The magnificated TEM images (Figure 2b-c) show the thicknesses of $NiCo_2O_4$ nanosheets are 5~10 nm and demonstrate that the $NiCo_2O_4$ NSs@HMRAs are porous. The high-resolution TEM (HRTEM) image of sample was measured as shown in Figure 2d, which displays the lattice fringes of a typical nanosheet in $NiCo_2O_4$ NSs@HMRAs, indicating the nanosheet possesses polycrystalline structure and consists of nanocrystals. The sizes of nanocrystals are 3~5 nm. These interplanar spacings in Figure 2d are determined to be 0.242 and 0.283 nm, which are identical with (311) and (220) lattice spacings of the spinel $NiCo_2O_4$, respectively. In addition, the selected-area electron diffraction (SAED) pattern shown in inset in Figure 2d also indicates the polycrystalline nature of the $NiCo_2O_4$ NSs@HMRAs. Figure 3a shows XRD pattern of the $NiCo_2O_4$ NSs@HMRAs. No diffraction peak of $NiCo_2O_4$ is seen besides the peaks of Ti substrate. This can be attributed to small nanocrystals in the $NiCo_2O_4$ NSs@HMRAs. In addition, no diffraction peak of ZnO is detected in the $NiCo_2O_4$ NSs@ HMRAs, indicating that the ZnO MRAs template is completely removed.

The $NiCo_2O_4$ NSs@HMRAs was further characterized by XPS measurements, through which we can obtain more detailed information about the oxidation state of transition metalion. The shift of the binding energy due to relative surface charging was corrected using the C 1s level at 284.6 eV as an internal standard. The fine XPS spectra of Ni 2p, Co 2p and O 1s are displayed in Figure 4a, 4b and 4c, respectively. In the Ni 2p spectrum (Figure 4a), two kinds of nickel species containing Ni^{2+} and Ni^{3+} are observed. The fitting peaks at 855.7 and 873.2 eV are indexed to Ni^{2+}, while those at 856.9 and 874.9 eV can be indexed to Ni^{3+}.[35] The satellite peaks at around 861.9 and 880.3 eV are two shake-up type peaks of

nickel at the high binding energy sides of the Ni $2p_{3/2}$ and Ni $2p_{1/2}$.[36-39] In the Co 2p spectra (Figure 4b), two kinds of Co species (Co^{2+} and Co^{3+}) are also detected. The binding energies at 780.1 and 795.1 eV are ascribed to Co^{3+}. Another two fitting peaks at 782.1 and 797.5 eV are ascribed to Co^{2+}.[40] The high resolution spect-rum for O1s (Figure 4c) shows three oxygen species marked as O1, O2 and O3. According to previous reports, the fitting peak of O1 at 529.7 eV is a typical metal-oxygen bond,[41] that of O2 at 531.2 eV corresponds to a high number of defect sites with low oxygen coordination in the material with small particle size,[42] and that of O3 at 532.6 eV can be ascribed to a multiplicity of physically and chemically bonded water on and within the surface.[41] The above XPS results demonstrate that the prepared $NiCo_2O_4$ NSs@HMRAs have a mixed compositions containing Co^{2+}, Co^{3+}, Ni^{2+} and Ni^{3+}, and they are in good agreement with the results reported for $NiCo_2O_4$ in the literatures [The $NiCo_2O_4$ is generally expressed as follows: $Co^{2+}{}_{1-x}Co^{3+}{}_{x}[Co^{3+}N^{i2+}{}_{x}\ Ni^{3+}{}_{1-x}]\ O_4(0\leq x\leq 1)$ (the cations within brackets are in octahedral sites and the outside ones are intetrahedral sites)].[14, 35-39, 43] EDS results of the $NiCo_2O_4$ NSs@HMRAs show the element ratio of Ni/Co is 1/1.86, which is close to the formula of $NiCo_2O_4$. This result is also confirmed by inductively coupled plasma atomic emission spectroscopy (ICP-AES).

Electrochemical impedance spectroscopy (EIS) was used to evaluate the ion diffusion and charge transmission in the $NiCo_2O_4$ NSs@HMRAs and it was measured at open circuit potential in the frequency range from 0.01 to 105 Hz. The Nyquist plot of $NiCo_2O_4$ NSs@HMRAs is shown in Figure 5a, which displays a linear part in the low-frequency region and a small semicircle in the high frequency region. The intercept at the real axis of the plot corresponds to the solution resistance (R_s) that is small and is only 0.75 Ω. The slope of a straight line in low frequency region can reflect the diffusive resistance resulting from the diffusion of active species in the electrolyte.[44-45] Herein, the $NiCo_2O_4$ NSs@HMRAs show almost vertical line in low frequency region as shown in Figure 5a, indicating the small diffusive resistance of electroactive species in electrolyte. This can be attributed to the special $NiCo_2O_4$ NSs@HMRAs structures with porous nanosheets and hollow microrod arrays. The diameter of conspicuous semicircle in the high-frequency range in EIS is associated with transmission of electrons, which is in accordance with

the faradic charge transfer resistance (R_{ct}).[46] Here the R_{ct} of the $NiCo_2O_4$ NSs@HMRAs is only about 0.5 Ω, which is much smaller than those reported for $NiCo_2O_4$ samples, such as the $NiCo_2O_4$ nanosheets (14.3 Ω)[47] and flower-like $NiCo_2O_4$ (16 Ω).[48] Therefore, the above results indicate the perfect ion diffusion and charge transmission in the $NiCo_2O_4$ NSs@HMRAs.

The $NiCo_2O_4$ NSs@HMRAs with high complexity in terms of structure and composition are expected to offer exciting opportunities for electrochemical energy stroage. The electrochemical properties of the $NiCo_2O_4$ NSs@HMRAs are firstly studied by cyclic voltammetry. Figure 5b shows CVs of the $NiCo_2O_4$ NSs@HMRAs electrode at various scan rates of 5~60 mV/s in 1. 0 M KOH aqueous solution. The shapes of these CVs clearly reveal the pseudocapacitive characteristics. A pair of redox peaks are clearly seen for all CVs within the potential range from 0 to 0.5 V *vs* SCE, which are associated with the faradaic redox reactions related to M-O/M-O-OH (where M refers to Ni or Co).[49] To learn about the charge storage capacity of the $NiCo_2O_4$ NSs@HMRAs, we carried out galvanostatic charge/discharge (GCD) measurements as shown in Figure 5c. Consistent with the CV results, the plateaus in GCD curves indicate the existence of Faradaic processes. The GCD curves of $NiCo_2O_4$ NSs@HMRAs are highly symmetrical without obvious i_R drop at low current densities, indicating a rapid *I-V* response and an excellent electrochemical reversibility. The C_{sp} *vs* scan rate and C_{sp} *vs* discharge current density are shown in Figure 5d and 5e, respectively. The reduction of C_{sp} at high scan rate and large current density can be attributed to the low diffusion of electrolyte ion. The ionic motion in electrolyte during the high rate charge-discharge process is always limited by diffusion because of the time constraint, and only the outer active surface is utilized for charge storage, so there is an obvious reduction in the electrochemical utilization of the electroactive materials at high scan rate and large current density. However, here the $NiCo_2O_4$ NSs@HMRAs still show large C_{sp} of 347 F/g at a large scan rate of 60 mV/s and 367 F/g at a high current density of 47 A/g, respectively. This can be attributed to the large specific surface area, fluent ionic channels and high proportion of active sites of the $NiCo_2O_4$ NSs@HMRAs because of the porous nanosheets and hollow microrod arrays, which can effectively improve the utilization and pseudocapacitance of electrode materials at high rates. Excellent cycling stability is also crucial for the real EC operations. Herein, the

long-term cycle stability of the $NiCo_2O_4$ NSs@HMRAs is evaluated by conducting 1500-cycle test at a high scan rate of 100 mV/s and it is shown in Figure 5f. The C_{sp} increases a little during the first 100 cycles and then slowly decreases. After 1500 cycles, the $NiCo_2O_4$ NSs@HMRAs show C_{sp} retention of 96.06%, indicating the excellent cycle stability.

To demonstrate the capacitive performance of $NiCo_2O_4$ NSs@HMRAs in a full cell set-up, the aqueous asymmetric supercapacitor (ASC) was assembled using $NiCo_2O_4$ NSs@HMRAs as positive electrode and AC as negative electrode as illustrated in Figure 6a. To determine the best operating potential of the ASC device, the CVs of $NiCo_2O_4$ NSs@HMRAs (black curve) and AC electrode (red curve) were measured in 1.0 M KOH solution, respectively, as shown in Figure 6b, which shows the potential windows of the $NiCo_2O_4$ NSs@HMRAs and AC electrodes are complementarity. Therefore, the $NiCo_2O_4$ NSs@HMRAs and AC electrodes are good candidates for the ASC device. The CVs shown in Figure 6c indicate that the potential window of the ASC can be as large as 1.5 V. To demonstrate the large potential window of the $NiCo_2O_4$ NSs@HMRAs//AC ASC, the CVs at 100 mV/s and GCD curves at 1.4 A/g were measured with different potential windows, and they are shown in Figure 6c and 6d, respectively. The aqueous $NiCo_2O_4$ NSs@HMRAs//AC ASC demonstrates an ideal capacitive behavior without obvious polarization curves, even at the potential window as large as 1.5 V. The enhancement of cell voltage will be a critical factor to improve the energy density of $NiCo_2O_4$ NSs@HMRAs//AC ASCs.

Figure 7a shows the CVs of the $NiCo_2O_4$ NSs@HMRAs//AC ASC at various scan rates. The oxidation peaks and reduction peaks on the CVs can be observed and the peak current becomes larger and larger with the scan rate increasing from 5 to 100 mV/s. However, there is no obvious distortion in CVs even at a high scan rate of 100 mV/s, indicating the good fast charge-discharge properties of the device.[50-51] The C_{sp} of the ASC based on the total mass of device was calculated from CVs according to equation (3). The C_{sp} of the $NiCo_2O_4$ NSs@HMRAs//AC ASC is 70.04 F/g at 5 mV/s and ~45.71% initial C_{sp} retention can be obtained when the scan rate is increased from 5 to 100 mV/s as shown in Figure 7b. In order to further evaluate the performance of the full cell, we also performed the GCD test at various current densities. As

illustrated in Figure 7c, the shapes of GCD curves for the $NiCo_2O_4$ NSs@HMRAs//AC ASC at different current densities tend to triangular-shaped curves, and the discharge curves are nearly linear and symmetric with the corresponding charge counterparts, suggesting rapid *I-V* response and good electrochemical reversibility.[48, 51] According to equation (4), the C_{sp} of the ASC is 49.3 F/g at 1.0 A/g and ~41.46% initial C_{sp} retention can be obtained when the current density is increased from 1.0 to 10.4 A g^{-1} as shown in Figure 7d. The GCD curves are also utilized to evaluate the power and energy densities of the $NiCo_2O_4$ NSs@HMRAs//AC ASC. Wich current density increasing from 1.0 to 10.4 A/g , the Ragone plot of the ASC is shown in Figure 7e, which shows the highest energy density is 15.42 Wh/kg and the highest power density is 7.8 kW/kg. In addition, the $NiCo_2O_4$ NSs@ HNRs//AC ASC shows high cycle stability even at a high scan rate of 100 mV/s as shown in Figure 7f (~106% of the initial C_{sp} after 2500 cycles), making it promising as one of the most attractive candidates for energy storage.

Conclusions

In conclusion, the novel $NiCo_2O_4$ NSs@HMRAs were fabricated via a simple and environmental friendly template-assisted electrodeposition followed by thermal annealing. The resulting products as electrodes exhibited predominant electrochemical properties and long-term cycle stability, which can be attributed to the hierarchical NSs@HMRAs superstructures grown on the current collectors: (*i*) the porous nanosheets can provide large surface area and accelerate the diffusion of active species; (*ii*) the hollow microrod arrays can act as ideal strain buffer to accommodate volum change and provide large specific surface area, fluent ionic channels and high proportion of active sites; (*iii*) the combination of cobalt and nickel anions in $NiCo_2O_4$ affords binary redox couples of Co^{2+}/Co^{3+} and Ni^{2+}/Ni^{3+} that will largely enhance the capacitive properties; (*iv*) the direct growth of $NiCo_2O_4$ on the current collector in a good contact can greatly enhance the conductivity. Additionally, the $NiCo_2O_4$ NSs@HMRAs//AC ASCs exhibit high C_{sp} of 70.04 F/g at 5 mV/s, high energy density of 15.42 Wh/kg, and excellent cycle stability. These findings suggest that the $NiCo_2O_4$ NSs@HMRAs are promising electrode materials for SCs with high performance and may open up great opportunities for electrochemical energy storage.

Acknowledgements

This work was supported by NSFC (51173212 and 21073240), Natural Science Foundation of Guangdong Province (S2013020012833), Fundamental Research Fund for the Central Universities (13lgpy51), Fund of New Star Scientist of Pearl River Science and Technology of Guangzhou (2011J2200057), SRF for ROCS, SEM ([2012]1707), and Open-End Fund of State Key Lab of Physical Chemistry of Solid Surfaces of Xiamen University (201113).

References

1. P.-C. Chen, G. Shen, Y. Shi, H. Chen, C. Zhou, *ACS Nano,* 2010, **4**, 4403-4411.
2. S. Chen, S.-Z. Qiao, *ACS Nano,* 2013, **7**, 10190-10196.
3. L. Huang, D. Chen, Y. Ding, S. Feng, Z. L. Wang, M. Liu, *Nano Lett.,* 2013, **13**, 3135-3139.
4. L. Huang, D. Chen, Y. Ding, Z. L. Wang, Z. Zeng, M. Liu, *ACS Appl. Mater. Interfaces,* 2013, **5**, 11159-11162.
5. Y. Wang, Y. Xia, *Adv. Mater.,* 2013, **25**, 5336-5342.
6. Y. Cheng, S. Lu, H. Zhang, C. V. Varanasi, J. Liu, *Nano Lett.,* 2012, **12**, 420-4211.
7. R. B. Rakhi, W. Chen, D. Cha, *Nano Lett.,* 2012, **12**, 2559-2567.
8. A. Sumboja, C. Y. Foo, X. Wang, P. S. Lee, *Adv. Mater.,* 2013, **25**, 2809-2815.
9. F. W. Richey, B. Dyatkin, Y. Gogotsi, Y. A. Elabd, *J. Am. Chem. Soc.,* 2013, **135**, 12818-12826.
10. J. Kang, A. Hirata, H.-J. Qiu, L. Chen, X. Ge, T. Fujita, M. Chen, *Adv. Mater.,* 2013, **25**, DOI: 10.1002/adma.201302975.
11. L.-F. Chen, Z.-H. Huang, H.-W. Liang, Q.-F. Guan, S.-H. Yu, *Adv. Mater.,* 2013, **25**, 4746-4752.
12. T. Y. Wei, H. Chen, H. C. Chien, S. Y. Lu, C. C. Hu, *Adv. Mater.,* 2010, **22**, 347-351.
13. H. Wang, Q. Gao, L. Jiang, *Small,* 2011, **7**, 2454-2459.
14. C. Yuan, J. Li, L. Hou, X. Zhang, L. Shen, X. W. Lou, *Adv. Funct. Mater.,* 2012**,** **22**, 4592-4597.
15. G. Zhang, H. Wu, H. E. Hoster, M. B. Chan-Park, X. W. Lou, *Energy Environ. Sci.,* 2012**,** **5**, 9453.
16. L. Hu, L. Wu, M. Liao, X. Hu, X. Fang, *Adv. Funct. Mater.,* 2012, **22**, 998-1004.
17. G. Zhang, X. W. Lou, *Sci. Rreports*, 2013, **3**, 1470.
18. C. Yuan, J. Li, L. Hou, J. Lin, X. Zhang, S. Xiong, *J. Mater. Chem. A,* 2013**,** **1**, 11145- 1151.
19. Q. Wang, B. Liu, X. Wang, S. Ran, L. Wang, D. Chen, G. Shen, *J. Mater. Chem.,* 2012**,** **22**, 21647.
20. X. Liu, S. Shi, Q. Xiong, L. Li, Y. Zhang, H. Tang, C. Gu, X. Wang, J. Tu, *ACS Appl. Mater. Interfaces,* 2013, **5**, 8790-8795.
21. J. Du, G. Zhou, H. Zhang, C. Cheng, J. Ma, W. Wei, L. Chen, T. Wang, *ACS Appl. Mater. Interfaces,* 2013, **5**, 7405-7409.
22. M. Liu, L. Kong, C. Lu, X. Li, Y. Luo, L. Kang, *ACS Appl. Mater. Interfaces* 2012, **4**, 4631-4636.
23. Z.-L. Wang, R. Guo, L.-X. Ding, Y.-X. Tong, G.-R. Li, *Sci. Reports,* 2013, **3**, 1204.
24. G. Xu, B. Ding, P. Nie, L. Shen, J. Wang, X. Zhang, *Chem.-Eur. J.,* 2013, **19**, 12306-12312.

25. L. Li, S. Peng, Y. Cheah, P. Teh, J. Wang, G. Wee, Y. Ko, C. Wong, M. Srinivasan, *Chem.-Eur. J.*, 2013, **19**, 5892-5898.
26. K. Wang, Q. Meng, Y. Zhang, Z. Wei, M. Miao, *Adv. Mater.*, 2013, **25**, 1494-1498.
27. M. Sathiya, A. S. Prakash, K. Ramesha, J.-M. Tarascon, A. K. Shukla, *J. Am. Chem. Soc.*, 2011, **133**, 16291-16299.
28. X. Zhang, W. Shi, J. Zhu, D. J. Kharistal, W. Zhao, B. Lalia, H. H. Hang, Q. Yan, *ACS Nano*, 2011, **5**, 2013-2019.
29. S. Dong, X. Chen, L. Gu, X. Zhou, L. Li, Z. Liu, P. Han, H. Xu, J. Yao, H. Wang, X. Zhang, C. Shang, G. Cui, L. Chen, *Energy Environ. Sci.*, 2011, **4**, 3502-3508.
30. F. Yang, J. Yao, F. Liu, H. He, M. Zhou, P. Xiao, Y. Zhang, *J. Mater. Chem. A*, 2013, **1**, 594-601.
31. M. Ye, D. Zheng, M. Lv, C. Chen, C. Lin, Z. Lin, *Adv. Mater.*, 2013, **25**, 3039-3044.
32. Y. Hou, Y. Cheng, T. Hobson, J. Liu, *Nano Lett.*, 2010, **10**, 2727-2733.
33. B. Zhao, S. Jiang, C. Su, R. Cai, R. Ran, M. O. Tadé, Z. Shao, *J. Mater. Chem. A*, 2013, **1**, 12310-12320.
34. J. Yan, Z. Fan, W. Sun, G. Ning, T. Wei, Q. Zhang, R. Zhang, L. Zhi, F. Wei, *Adv. Funct. Mater.*, 2012, **22**, 2632-2641.
35. J. Kim, D. Pugmire, D. Battaglia, M. Langell, *Applied Surf. Sci.*, 2000, **165**, 70-84.
36. J. Xiao, S. Yang, *J. Mater. Chem.*, 2012, **22**, 12253-12262.
37. P. V. Kamath, G. H. Annal Therese, J. Gopalakrishnan, *J. Solid State Chem.*, 1997, **128**, 38-41.
38. M. M. Natile, A. Glisenti, *Chem. Mater.*, 2002, **14**, 4895-4903.
39. Y. Roginskaya, O. Morozova, E. Lubnin, Y. E. Ulitina, G. Lopukhova, S. Trasatti, *Langmuir*, 1997, **13**, 4621-4627.
40. J. Marco, J. Gancedo, M. Gracia, J. Gautier, F. Berry, *Journal of Solid State Chem.*, 2000, **153**, 74-81.
41. T. Choudhury, S. Saied, J. Sullivan, A. Abbot, *J. Physics D: Applied Physics*, 1989, **22**, 1185-1188.
42. V. Jiménez, A. Fernández, J. Espinós, A. González-Elipe, *J. Electron Spectroscopy Related Phenomena*, 1995, **71**, 61-71.
43. C. Yuan, J. Li, L. Hou, L. Yang, L. Shen, X. Zhang, *J. Mater. Chem.*, 2012, **22**, 16084-16090.
44. J. Lang, X. Yan, W. Liu, R. Wang, Q. Xue, *J. Power Sources*, 2012, **204**, 220-229.
45. M. Li, S. Xu, T. Liu, F. Wang, P. Yang, L. Wang, P. Chu, *J. Mater. Chem. A*, 2013, **1**, 532-540.
46. P. Justin, S. K. Meher, G. R. Rao, *J. Phys. Chem. C*, 2010, **114**, 5203-5210.
47. L. Li, Y. Cheah, Y. Ko, P. Teh, G. Wee, C. Wong, S. Peng, M. Srinivasan, *J. Mater. Chem. A*, 2013, **1**, 10935-10941.
48. X. Lu, X. Huang, S. Xie, T. Zhai, C. Wang, P. Zhang, M. Yu, W. Li, C. Liang, Y. Tong, *J. Mater. Chem.*, 2012, **22**, 13357-13364.
49. F. Zhang, C. Yuan, X. Lu, L. Zhang, Q. Che, X. Zhang, *J. Power Sources*, 2012, **203**, 250-256.
50. X. Wang, A. Sumboja, M. Lin, J. Yan, P. S. Lee, *Nanoscale*, 2012, **4**, 7266-7272.
51. Z. Fan, J. Yan, T. Wei, L. Zhi, G. Ning, T. Li, F. Wei, *Adv. Funct. Mater.*, 2011, **21**, 2366-2375.

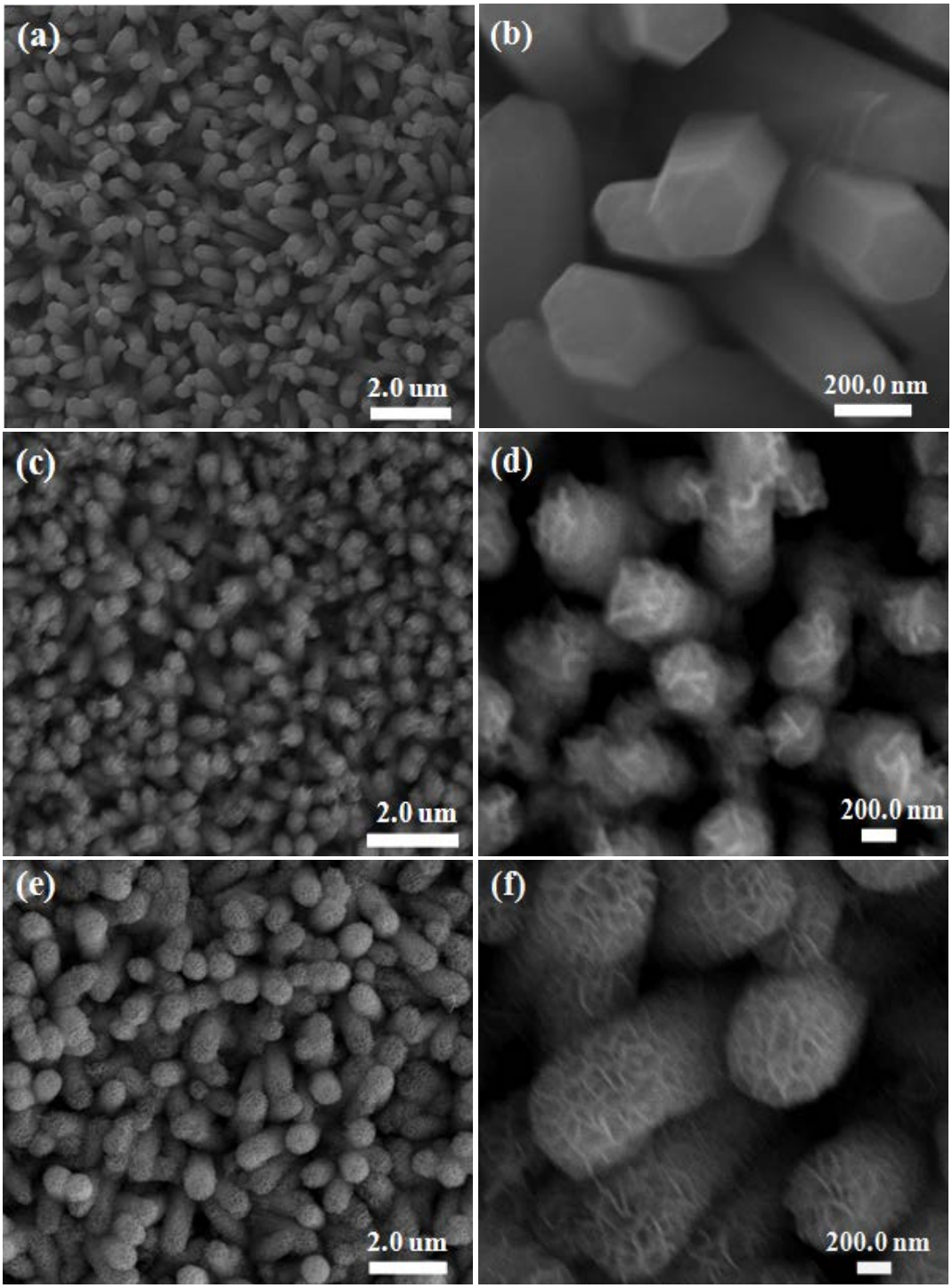

Figure 1. SEM images of (a-b) ZnO MRAs; (c-d) ZnO@$Ni(OH)_2$/$Co(OH)_2$ MRAs; and (e-f) $NiCo_2O_4$ NSs@ HMRAs.

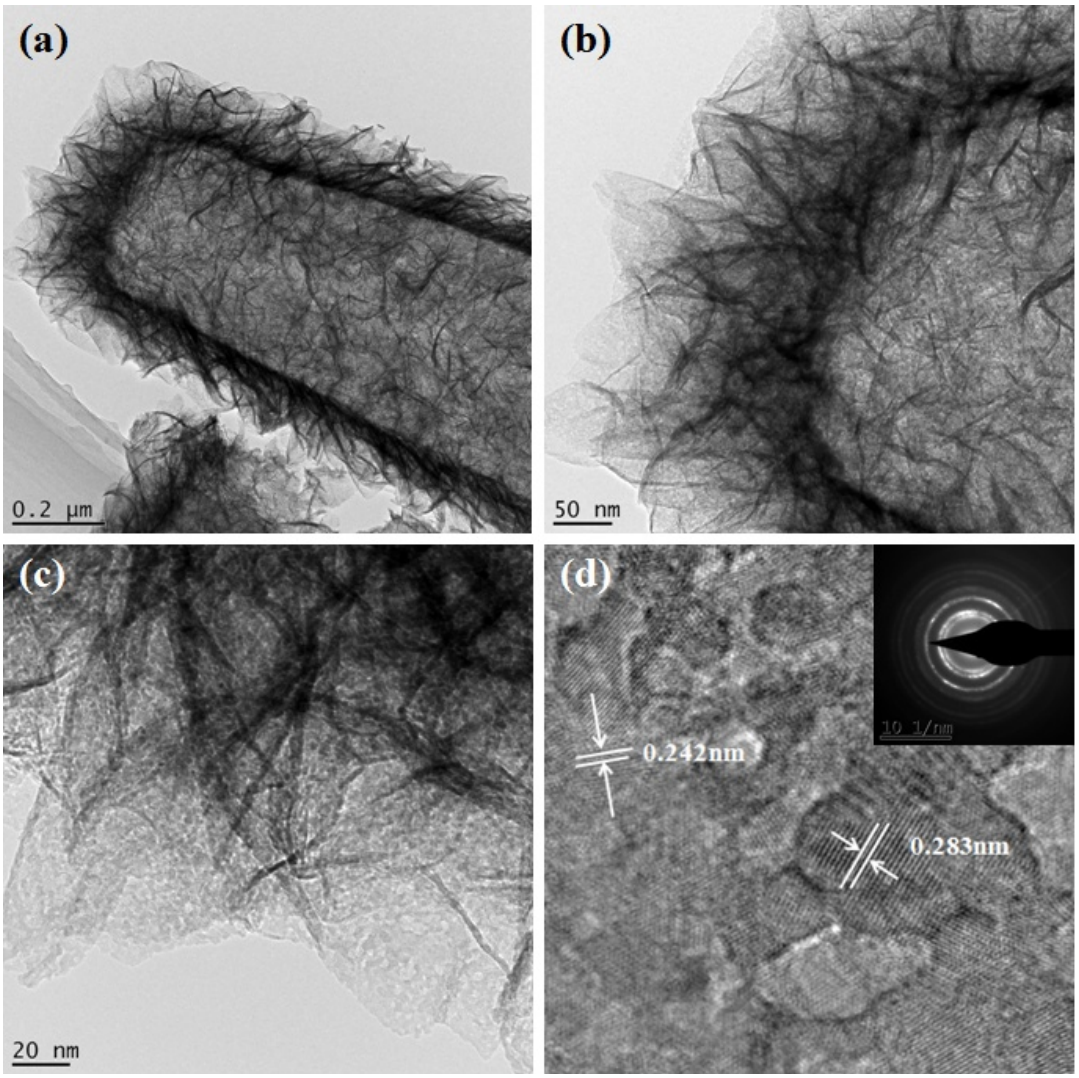

Figure 2. (a-c) TEM images and (d) HTEM image of $NiCo_2O_4$ NSs@HMRAs. The insert in (d) is the corresponding SAED pattern.

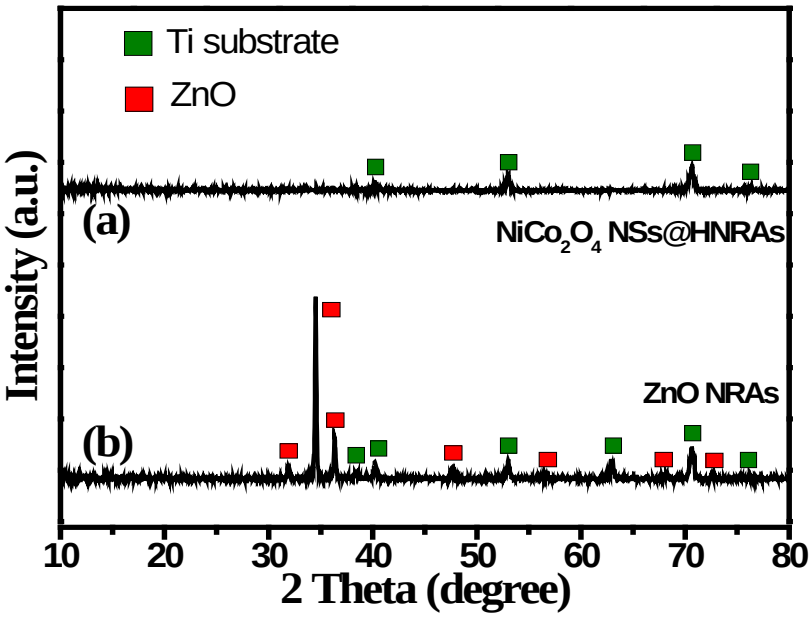

Figure 3. XRD patterns of (a) $NiCo_2O_4$ NSs@HMRAs and (b) ZnO MRAs on Ti substrates.

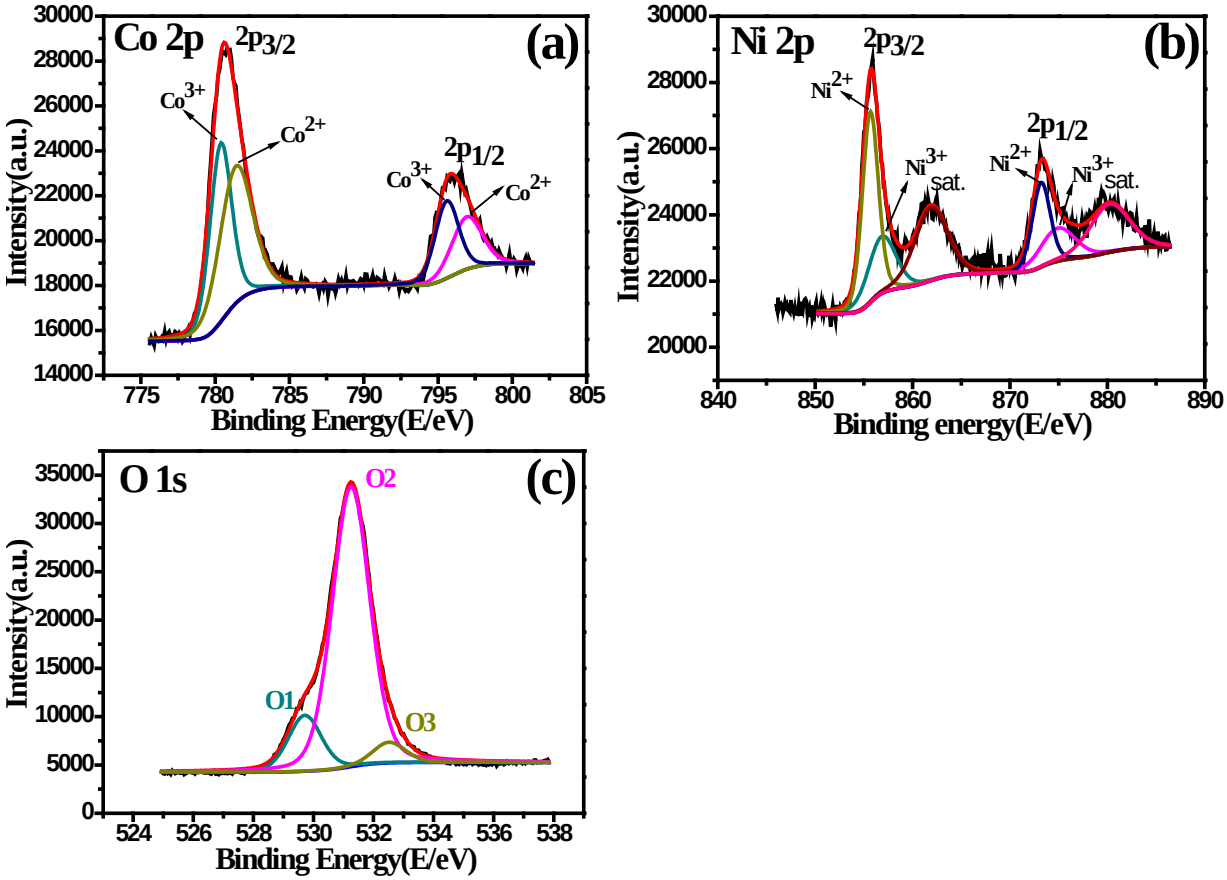

Figure 4. (a) Ni 2p; (b) Co 2p; and (c) O1s XPS spectra of the as-prepared $NiCo_2O_4$ NSs@HMRAs.

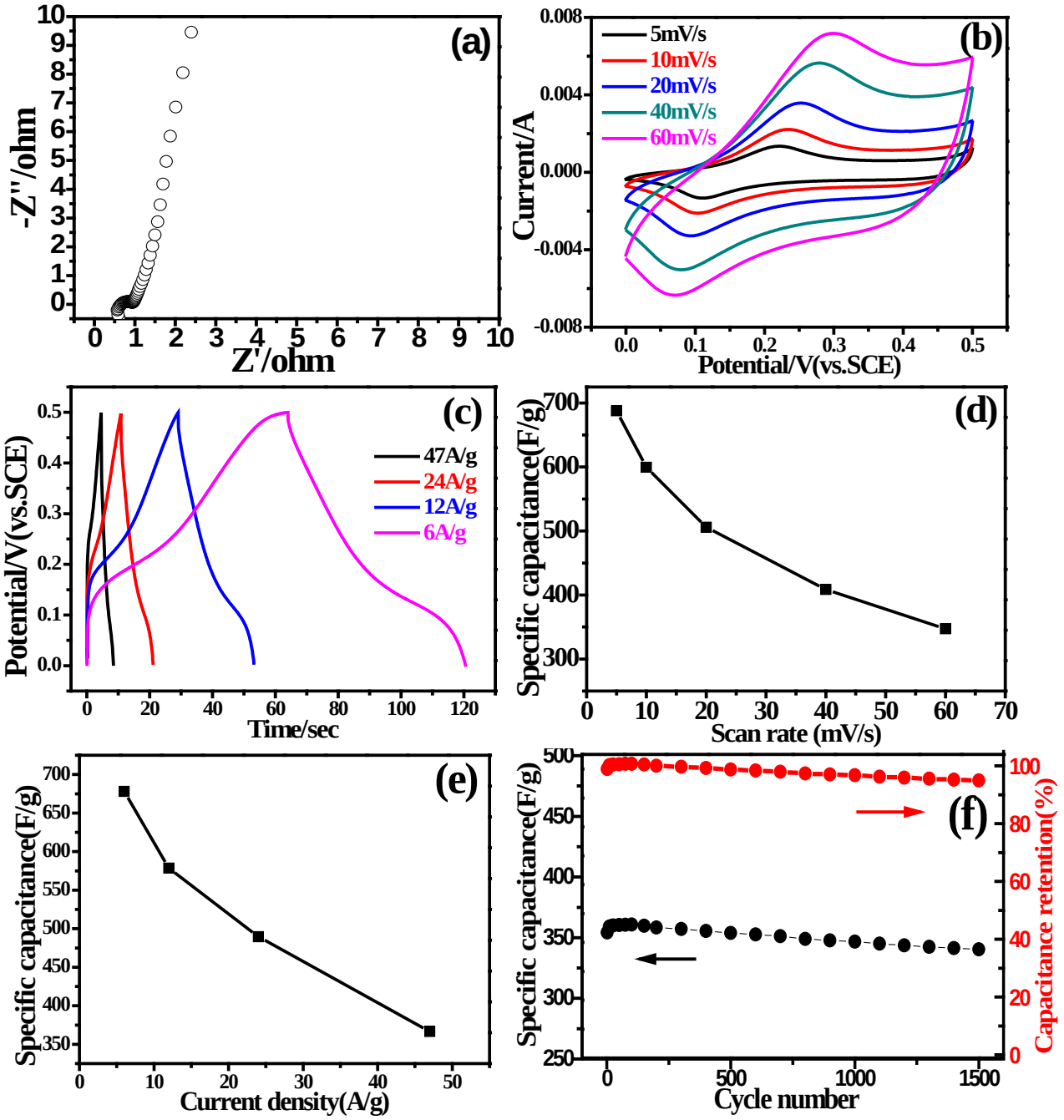

Figure 5. Electrochemical performances of the $NiCo_2O_4$ NSs@HMRAs electrodes: (a) EIS measured at the open circuit potential in the frequency range from 0.01 to 105 Hz; (b) CVs at different scan rates; (c) GCD curves at different current densities; (d) C_{sp} calculated from CVs as a function of scan rate; (e) C_{sp} calculated from GCD curves as a function of current density; (f) cycling performances during 1500 cycles at a high scan rate of 100 mV/s. The mass of $NiCo_2O_4$ NSs@HMRAs electrode is 0.17 mg.

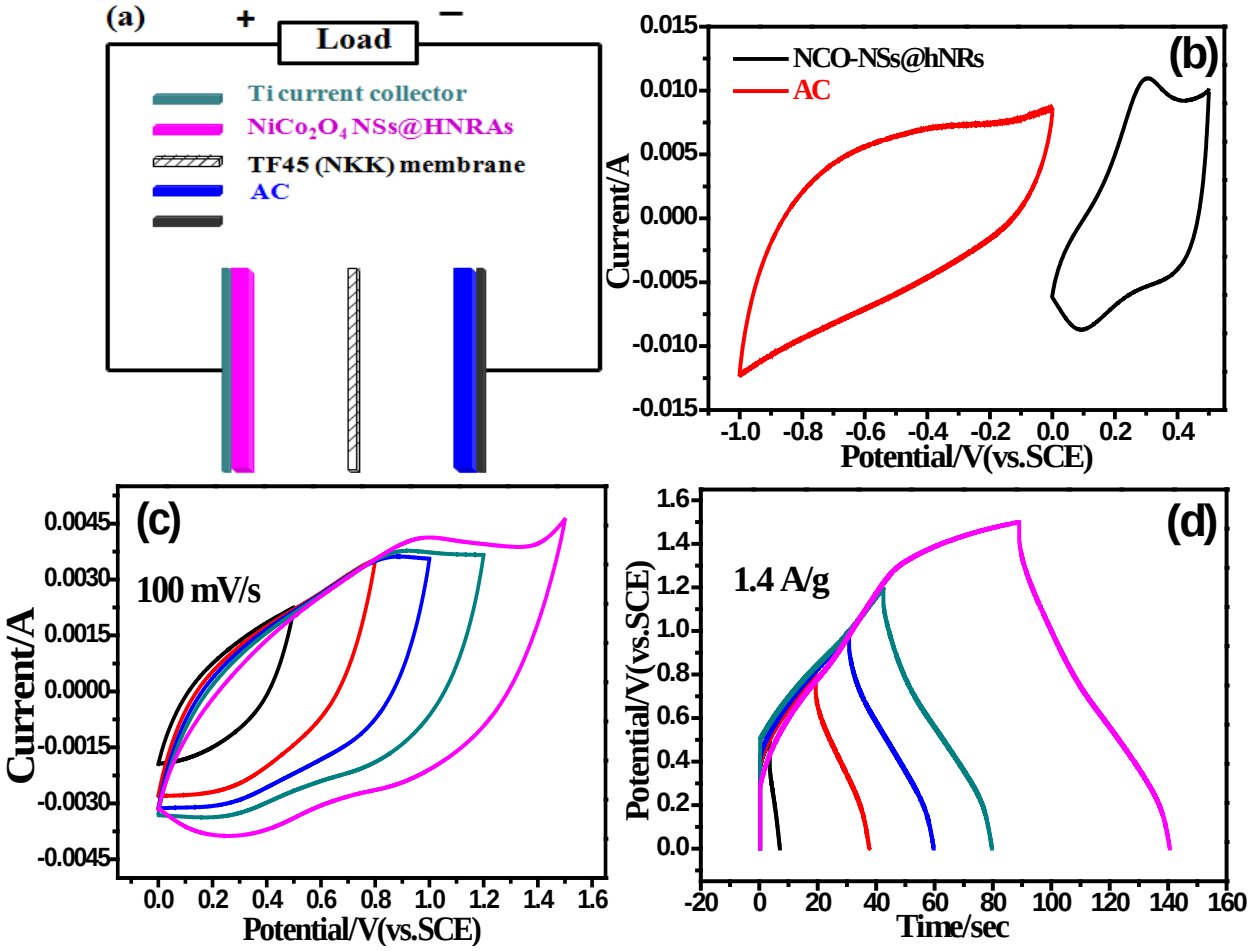

Figure 6. (a) Schematic illustration of the ASC device composed of the $NiCo_2O_4$ NSs@HMRAs and AC electrodes. The two electrodes are separated by the TF45 (NKK) membrane (separator); (b) CVs of the $NiCo_2O_4$ NSs@HMRAs and AC electrodes collected at 100 mV/s in a three-electrode system; (c) CVs of the ASC device collected at different potential windows at 100 mV/s; (d) GCD curves of the ASC device collected at different potential windows at a fixed current density of 1.4 A/g.

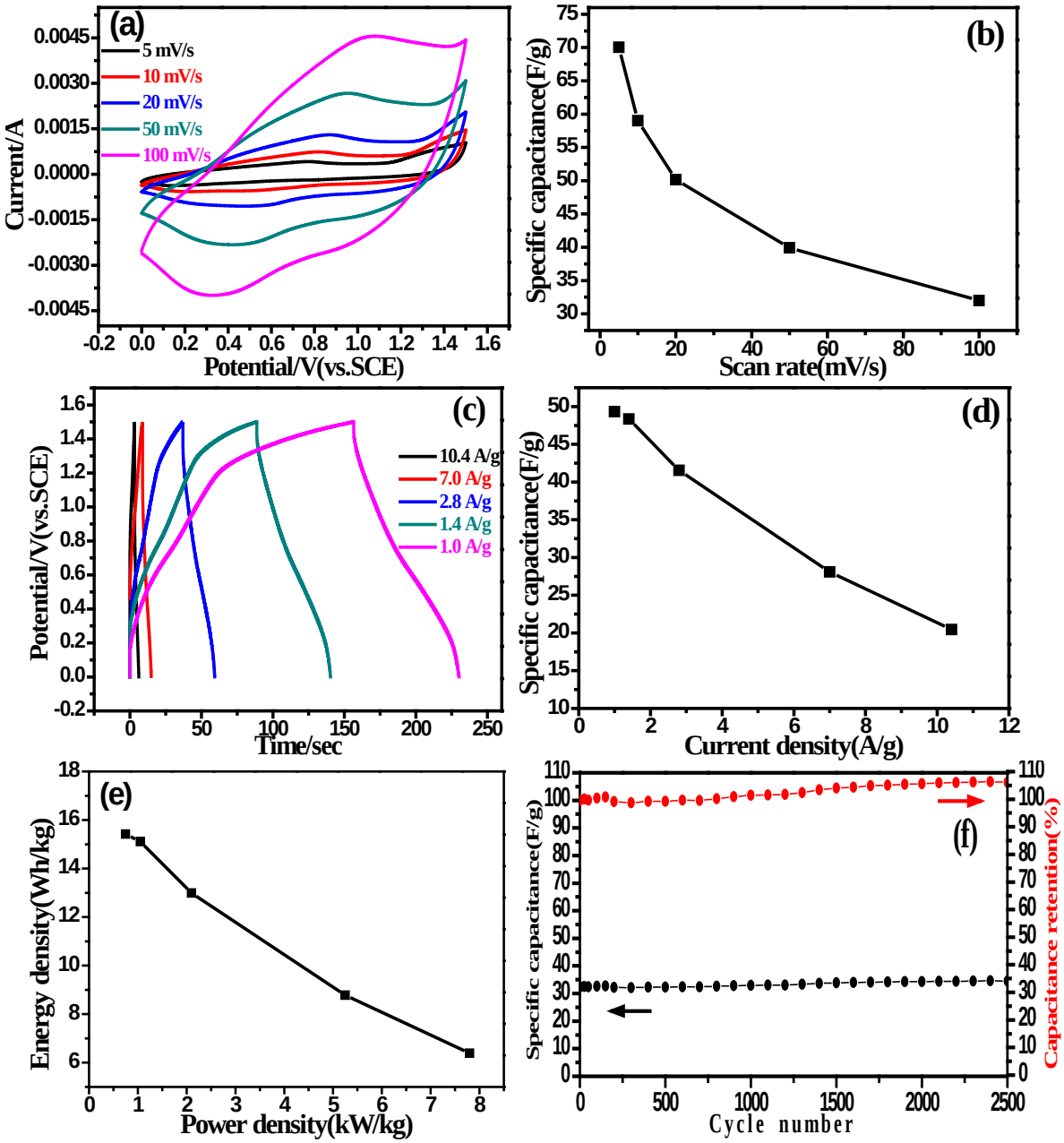

Figure 7. Electrochemical performances of the $NiCo_2O_4$ NSs@HMRAs//AC ASC: (a) CVs at different scan rates; (b) C_{sp} calculated from CVs as a function of scan rate; (c) GCD curves at different current densities; (d) C_{sp} calculated from GCD curves as a function of current density; (e) Ragone plot; (f) cycling performances during 2500 cycles at a high scan rate of 100 mV/s.

TOC GRAPHICS

Novel $NiCo_2O_4$ NSs@HNRAs are fabricated via a simple and environmental friendly template-assisted electrodeposition followed by thermal annealing and they exhibit predominant electrochemical properties and long-term cycle stability.